# Acoustic Black Holes and Superressonance Mechanisms

**Extended abstract**

Sofia Freitas[1]

[1] *CENTRA, Departamento de Física, Instituto Superior Técnico – IST, Universidade de Lisboa – UL, Avenida Rovisco Pais 1, 1049 Lisboa, Portugal*

(Dated: October 17, 2017)

It has been showed that sound waves, in a moving fluid, behave analogously to scalar fields in a curved spacetime. Supersonic fluid flow can generate a "dumb hole", which corresponds to a region in space from which no information can be extracted. This is the analogue of a black hole in the theory of General Relativity. The formal mathematical equivalence is very powerful once it allows for the study of black holes in laboratories. Throughout this work, we study the analogue gravity description of rotating black holes, with a focus on superradiance. We analyse two distinct spacetimes: the draining bathtub and the rotating cylinder setups. Viscosity is also included on the latter.

## I. INTRODUCTION

Black holes (BHs) are described by the theory of General Relativity (GR). GR was developed in 1915 by Albert Einstein and it describes gravity as the curvature of spacetime. In 1904, Einstein was troubled by the views of relativity put forward by Galileo and Maxwell. On the one hand, Galileo claimed that absolute motion could not be defined. Maxwell's electromagnetism, on the other, established that light travelled at a fixed speed $c$. Einstein came to the conclusion these two notions could only be compatible if $c$ were to be kept constant across different frames of reference. The subsequent view that time was not absolute made way for the establishment of Special Relativity. GR arose years later, expanding the theory to account for effects of acceleration. The latter passed its first test in 1919, when the bending of star light was observed during a solar eclipse [1]. Since then, the theory has been put to test in several other occasions, the latest being the experimental detection of gravitational waves in 2015 [2]. In a nutshell, GR is defined via Einstein's field equations,

$$G_{\mu\nu} = R_{\mu\nu} - \frac{1}{2}Rg_{\mu\nu} = 8\pi T_{\mu\nu}, \tag{1}$$

which describe how matter and energy interact with spacetime, the fabric of our universe. The Ricci tensor $R_{\mu\nu}$ and the Ricci scalar $R = g^{\mu\nu}R_{\mu\nu}$ are geometrical entities which measure the curvature of spacetime. They depend solely on the metric $g_{\mu\nu}$. The element on the right hand side of the equation, $T_{\mu\nu}$, is the stress-energy tensor and it accounts for the presence and distribution of matter. The first solution to Einstein's field equations is due to Karl Schwarzschild who, in 1916, computed the gravitational field generated by a static point mass [3]. Subsequently, other solutions have been discovered. A particularly relevant one for this work is the Kerr solution, which describes a rotating BH.

Despite its extremely interesting features, astrophysical BHs are of difficult observation and direct study. That is why one must rely on other, secondary, effects. A very important secondary effect is the Penrose process. Theorised in 1969 by Roger Penrose, it accounts for the loss of angular momentum in rotating BHs. Penrose argued that once particles entered a special region of the BH, called the ergosphere, they could be scattered and ejected with greater energy than the one they had initially. Note that this scattering process rarely occurs, as very specific conditions must be verified. For instance, one must arrange the initial trajectory such that afterwards there is a geodesic trajectory that takes the particle back outside the ergoregion. Nonetheless, the Penrose process was central in the establishment of its analogue wave process, superradiance. Superradiance is a radiation enhancement process that occurs in dissipative systems. In BHs, it happens at the level of the event horizon. Superradiance allows for energy and angular momentum to be extracted from the vacuum, resulting in a consequent amplification of the scattered wave packet. Superradiance in rotating BHs was first discovered in 1971, by Zel'dovich. He showed, provided the superradiance condition is satisfied, that the scattering of incident waves in rotating dissipative bodies resulted in an amplification of such waves, producing outgoing waves of larger amplitude. The superradiance condition reads

$$\omega < m\Omega, \tag{2}$$

where $\omega$ is the frequency of the incident radiation, $m$, the azimuthal number, accounts for the projection of the angular momentum along the axis of rotation and $\Omega$ is the angular velocity of the body.

In 1981, Unruh showed that sound waves, in a moving fluid, behave the same way as scalar fields in curved spacetimes [4]. He observed horizons could occur in day-to-day situations and drew analogies between fluid mechanics and GR. He called these horizons "dumb holes", and proved their existence as a consequence of supersonic fluid flows, as illustrated in Figure 1. By finding ways to reproduce behaviours of BHs and other astrophysical bodies, one is able to carry out experiments in laboratories, with the aim of testing the existing theories. A leading laboratory in the field is the Quantum Gravity Laboratory in Nottingham. In a recent article [5], Silke Weinfurtner's team describes the first laboratory

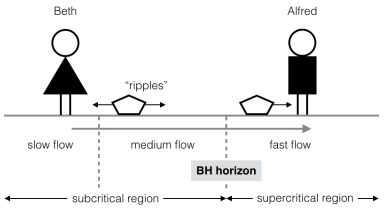


FIG. 1. Propagation of information using the analogue fluid mechanics. Beth and Alfred communicate using "ripples" (acoustic disturbances) on the free surface of the fluid. The fluid naturally flows from Beth to Alfred, so she is always able to get her message across. For Alfred to be able to reply to Beth, he must be able to guarantee the ripples he sends move faster upstream than the flow does downstream. But Alfred is in a supercritical region, so he can never send any information upstream – nothing can counterpropagate the flow in this region. The region separating the sub and supercritical regions is the analogue BH horizon.

detection of superradiance. By working with a draining bathtub fluid flow, they observed that plane waves propagating on the surface of the water were amplified after being scattered off by the draining vortex. The experimental setup in Nottingham was first described in 2002 by Unruh and Schützhold [6]. They proposed an experiment in which superradiance could be detected in the laboratory by assuming a long wavelength, shallow water approximation. An alternative experimental setup worth mentioning is the one proposed by Cardoso et al., in 2016 [7]. The authors analysed the hypothesis of mimicking the vortex geometry by making use of a rotating cylinder. They showed that, given an appropriate choice of material for the cylinder, surface and sound waves were amplified. Both proposals are studied here.

## II. ACOUSTIC ANALOGUES

### A. Fluid dynamics

In 1981, Unruh developed a method for mapping certain aspects of BH physics into fluid mechanics. He started by considering a barotropic and inviscid fluid, whose flow is irrotational – though possibly time dependent. The equation of motion for the velocity potential describing an acoustic disturbance is identical to the d'Alembertian equation of motion for a minimally-coupled massless scalar field $\psi$, propagating in a $(1+3)$-dimensional Lorentzian geometry, namely

$$\Delta\psi = \frac{1}{\sqrt{-g}}\left(\partial_\mu\sqrt{-g}g^{\mu\nu}\partial_\nu\psi\right) = 0. \tag{3}$$

This is just the Klein Gordon equation, $\nabla_\mu\nabla^\mu\psi = 0$, describing the dynamics of a scalar field. Under these conditions, the propagation of sound is governed by an acoustic metric $g_{\mu\nu}(t,\mathbf{x})$, which depends algebraically on the density and velocity of the flow and on the local speed of sound in the fluid:

$$g_{\mu\nu}(t,\mathbf{x}) = \frac{\rho}{c}\begin{pmatrix} -(c^2 - ||\mathbf{v}||^2) & -\mathbf{v}^{\mathrm{T}} \\ -\mathbf{v} & I_{[3\times3]} \end{pmatrix}, \tag{4}$$

where $I_{[3\times3]}$ is the $3\times3$ identity matrix. In general, when the fluid is non-homogeneous and flowing, the acoustic Riemann tensor associated with the acoustic metric is non-zero.

The path to arrive at this result is described promptly. One starts by writing down the two fundamental equations ruling fluid dynamics, the continuity equation and the Euler equation. Respectively, they read:

$$\partial_t\rho + \nabla\cdot(\rho\mathbf{v}) = 0 \tag{5}$$

$$\rho\frac{d\mathbf{v}}{dt} = \rho\left[\partial_t\mathbf{v} + (\mathbf{v}\cdot\nabla)\mathbf{v}\right] = \mathbf{F}, \tag{6}$$

where $\rho$ is the density of the fluid and $\mathbf{v}$ is the fluid velocity vector field. $\mathbf{F}$ in the Euler equation is defined as

$$\mathbf{F} = -\nabla p - \rho\nabla\Phi, \tag{7}$$

$p$ being the pressure and $\Phi$ the potential of an external driving force. We assume the fluid to be vorticity free, i.e. locally irrotational. This means the velocity can be written as $\mathbf{v} = \nabla\psi$. Furthermore, the fluid is assumed to be barotropic, meaning the fluid's equation of state is of the form $\rho = \rho(p)$. The latter is helpful in defining the specific enthalpy $h$,

$$\nabla h = \frac{1}{\rho}\nabla p. \tag{8}$$

The Euler equation (6) can thus be written as

$$\partial_t\psi + h + \frac{1}{2}(\nabla\psi)^2 + \Phi = 0. \tag{9}$$

Next, one linearises the fundamental equations around an average bulk motion described by the background dynamical quantities $(p_0, \rho_0, \psi_0)$, plus some low amplitude acoustic perturbations $(\varepsilon p_1, \varepsilon\rho_1, \varepsilon\psi_1)$. We consider only first order terms in $\varepsilon$.

$$p = p_0 + \varepsilon p_1 + \mathcal{O}(\varepsilon^2), \qquad \rho = \rho_0 + \varepsilon\rho_1 + \mathcal{O}(\varepsilon^2),$$
$$\psi = \psi_0 + \varepsilon\psi_1 + \mathcal{O}(\varepsilon^2). \tag{10}$$

The continuity and the Euler equations can be rewritten as two versions of themselves: an unperturbed and a perturbed one. The unperturbed equations will simply be the aforementioned equations (5) and (9), while the perturbed equations read

$$\text{Continuity equation:} \quad \partial_t\rho_1 + \nabla\cdot(\rho_1\mathbf{v_0} + \rho_0\mathbf{v_1}) = 0 \tag{11}$$

$$\text{Euler equation:} \quad \partial_t\psi_1 + h_1 + \mathbf{v_0}\nabla\psi_1 = 0. \tag{12}$$

The perturbation to the enthalpy can be identified as $h_1 = \frac{p_1}{\rho_0}$ via a Taylor expansion. Making use of equation (12), the following relation arises:

$$p_1 = -\rho_0\left(\partial_t\psi_1 + \mathbf{v_0}\nabla\psi_1\right). \tag{13}$$

Together with the barotropic assumption

$$p = p(\rho) \implies p_1 = \frac{\partial p}{\partial \rho}\rho_1 \tag{14}$$

and equation (11), one obtains the wave equation,

$$\partial_t \left(\rho_0(\partial_t\psi_1 + \mathbf{v_0}\cdot\nabla\psi_1)\right) + \nabla\cdot\left(-c^2\rho_0\nabla\psi_1 + \rho_0\mathbf{v_0}(\partial_t\psi_1 + \mathbf{v_0}\cdot\nabla\psi_1)\right) = 0, \tag{15}$$

where the local speed of sound has been defined as

$$c^{-2} = \frac{\partial\rho}{\partial p}. \tag{16}$$

This wave equation describes the propagation of the linearised scalar potential $\psi_1$. Once $\psi_1$ is computed, $p_1$ and $\rho_1$ are easily calculated via equations (13) and (14). Thus, the wave equation completely determines the propagation of the acoustic disturbances $(p_1, \rho_1, \psi_1)$. The background fields $(p_0, \rho_0, \psi_0)$, which appear as time-dependent and position-dependent coefficients in the equation, are constrained to solve the equations of fluid motion for an externally-driven, barotropic, inviscid, and irrotational flow. The corresponding acoustic metric is given by equation (4).

### B. Vortex geometries: the draining bathtub fluid flow

The first setup analysed consists of a draining bathtub flow, similar to the ones we see everyday in wash basins. Without any loss of generality, one describes the vortex geometry in polar coordinates: $(t, r, \theta)$. The background fluid velocity can be written as

$$\mathbf{v_0} = \frac{A\mathbf{e_r} + B\mathbf{e}_\theta}{r}, \tag{17}$$

with the corresponding potential

$$\psi_0(r,\theta) = A\log(r/a) + B\theta. \tag{18}$$

$A$ and $B$ are parameters associated to the radial and angular components of the background fluid velocity, and $a$ is some irrelevant length scale. For a derivation of this result please refer to Reference [8]. Observe that $A$ can be either positive or negative: $A < 0$ corresponds to a sink and $A > 0$ to a source. Respectively, they will either emulate a future acoustic horizon – acoustic black hole – or a past acoustic horizon – acoustic white hole.

Dropping a position independent prefactor, the line element describing the propagation of sound waves in the $(1+2)$-dimensional draining bathtub fluid flow reads

$$ds^2 = -\left(c^2 - \frac{A^2+B^2}{r^2}\right)dt^2 - \frac{2A}{r}dtdr - 2Bdtd\theta + dr^2 + r^2d\theta^2. \tag{19}$$

The coordinates for the horizon and ergosphere of the spacetime are

$$r_H = \frac{|A|}{c} \tag{20}$$

$$r_e = \frac{\sqrt{A^2+B^2}}{c}. \tag{21}$$

## III. DYNAMICS OF ACOUSTIC HOLES

### A. Wave equation

In order to obtain the wave equation ruling the behaviour of sound waves in the draining bathtub flow, we recover the general result of equation (15) and use the background fluid flow velocity presented in equation (17):

$$\partial_t^2\psi_1 + \left(\frac{A}{r}\partial_r + \frac{B}{r^2}\partial_\theta\right)\partial_t\psi_1 - \frac{c^2}{r^2}(\partial_r(r\partial_r\psi_1) + \partial_\theta^2\psi_1) = 0. \tag{22}$$

The ansatz of a plane wave,

$$\psi_1(t,r,\theta) = R(r)e^{-i(\omega t - m\theta)}, \tag{23}$$

allows one to separate the wave equation. We work only with the radial part. Writing $R(r) = Z(r)H(r)$ and requiring $Z(r)$ to solve

$$Z_{,r} + \frac{1}{2}\frac{(c^2r^2 - A^2) + 2iA(Bm - r^2\omega)}{r(c^2r^2 - A^2)}Z = 0, \tag{24}$$

one obtains the Schroedinger-like wave equation:

$$H_{,r_*r_*} + \left[c^{-2}\left(\omega - \frac{Bm}{r^2}\right)^2 - \frac{c^2r^2 - A^2}{c^2r^2}\left(r^{-2}\left(m^2 - \frac{1}{4}\right) + \frac{5A^2}{4r^4c^2}\right)\right]H = 0. \tag{25}$$

Observe the introduction of the tortoise coordinate $r_*$

$$\frac{dr_*}{dr} = \Delta = \left(1 - \frac{A^2}{c^2r^2}\right)^{-1}, \tag{26}$$

which explicitly reads

$$r_* = r + \frac{A}{2c}\log\left|\frac{cr - A}{cr + A}\right|. \tag{27}$$

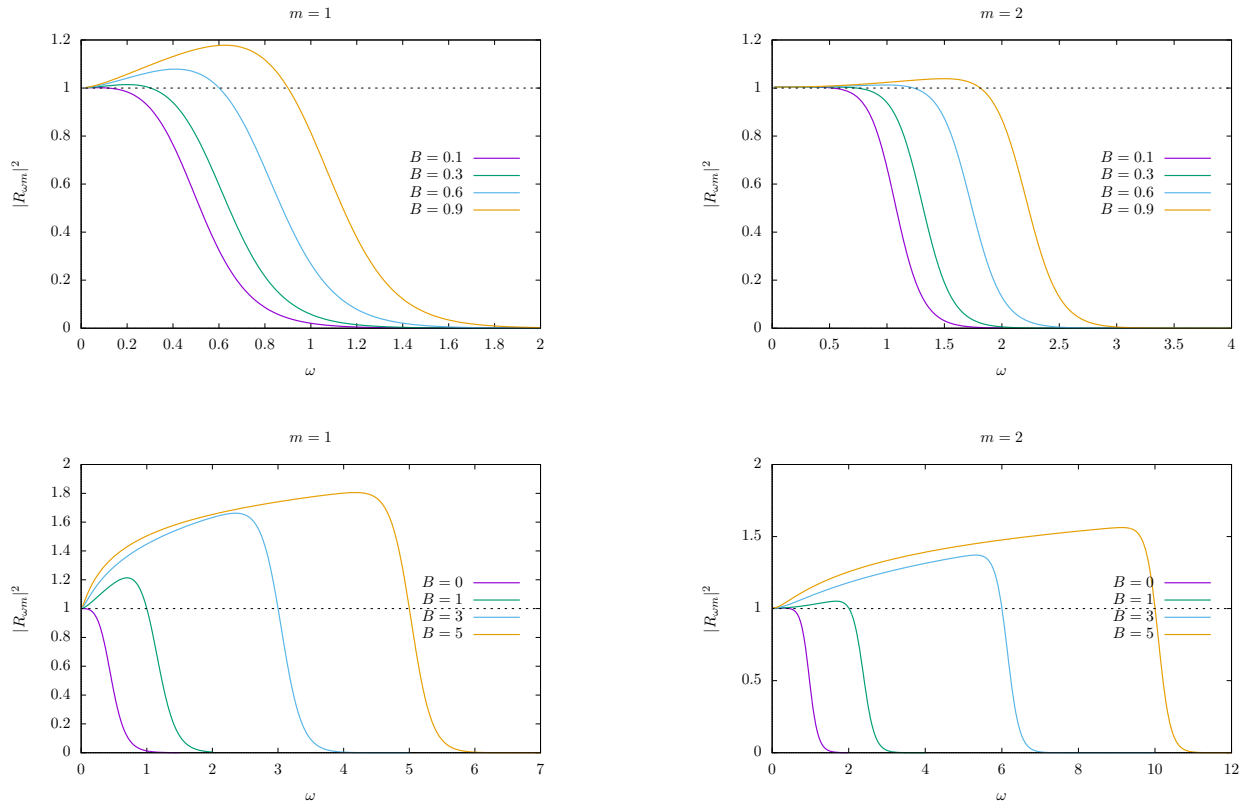


FIG. 2. Reflection coefficient $|R_{\omega m}|^2$ as a function of $\omega$. Several solutions for the differential equation are produced, as one changes the value of parameter $B$, the angular velocity at the horizon. The left hand panels show the results for $m = 1$ and the right hand ones the results for $m = 2$. $|R_{\omega m}|^2 = 1$ (limit above which superradiance occurs) is plotted as a dashed line.

Using the rescaled quantities $\hat{r} = \frac{rA}{c}$, $\hat{\omega} = \frac{\omega A}{c^2}$ and $\hat{B} = \frac{B}{A}$, the wave equation reads

$$H_{\hat{r}_*,\hat{r}_*} + Q(\hat{r})H = 0. \tag{28}$$

The potential is

$$Q = \left(\hat{\omega} - \frac{\hat{B}m}{\hat{r}^2}\right)^2 - V(\hat{r}) \tag{29}$$

$$V = \frac{\hat{r}^2 - 1}{\hat{r}^2}\left(\hat{r}^{-2}\left(m^2 - \frac{1}{4}\right) + \frac{5}{4\hat{r}^4}\right). \tag{30}$$

From here onwards, all hats are dropped and one works only with the rescaled quantities. In such units, the horizon and ergosurface occur at the following radii:

$$r_H = 1, \qquad r_e = \sqrt{1 + B^2}. \tag{31}$$

### B. Scattering in the vortex geometry. Superradiance

The complicated form of the potential given by equation (29) rules out an analytical solution that holds for the entire domain. However, it is possible to obtain analytical solutions at the horizon, $r_H = 1$, and at infinity, $r_\infty \to \infty$. They read

$$H_H = A_H e^{-i(\omega - Bm)r_*} \tag{32}$$

$$H_\infty = A_{\text{in}} e^{-i\omega r_*} + A_{\text{out}} e^{i\omega r_*}. \tag{33}$$

The Wronskian associated to $H$ and $H^\dagger$ is constant in the radial coordinate[1]. This means one can equate the horizon and infinity Wronskians, resulting in an energy conservation condition. Such equality, together with the superradiance condition[2] $\omega < mB$, yields the result

$$\left|\frac{A_{\text{out}}}{A_{\text{in}}}\right|^2 > 1. \tag{34}$$

Observe this ratio is, by definition, the reflection coefficient $|R_{\omega m}|^2$.

[1] In Schroedinger-like real-valued effective potential equations, the Wronskian is conserved in the coordinate upon which the wave equation is being differentiated.

[2] In the draining bathtub spacetime, the angular velocity at the event horizon is given by the quantity $B$.

Next, one works with the wave equation

$$\left(1-\frac{1}{r^2}\right)^2\frac{d^2H}{dr^2}+\frac{2}{r^3}\left(1-\frac{1}{r^2}\right)\frac{dH}{dr}+Q(r)H=0, \quad (35)$$

where the derivatives have all been written with respect to the radial coordinate $r$. The numerical method used to solve the wave equation consists in iteratively integrating it for different frequencies $\omega$, imposing the boundary conditions expressed by equations (32) and (33). The output of each cycle consist of a pair of points $(\omega, |R_{\omega m}|^2)$, which is later plotted. A series expansion with the aim of increasing precision near the boundaries is performed. The incoming wave is normalised by setting $A_H = 1$ in equation (32).

In Figure 2, we present some of the plots that illustrate the results produced. In the plots, we have included a dashed line at $|R_{\omega m}|^2 = 1$. This line sets the frontier between the cases of no amplification and amplification. Whenever the curves are above the dashed line, there is superradiant scattering. It is interesting to note that the intersection of each curve with the horizontal line happens when $\omega = mB$, as predicted by the theory. Out of the parameters chosen, the maximum value obtained for amplification was $|R_{\omega m}|^2 = 1.805$ for $\omega = 4.18$, $m = 1$ and $B = 5$. Larger amplification is obtained for larger values of the rotation parameter $B$. Once rotation is the source of amplification in superresonant mechanisms, it is natural that the greater the rotational speed, the greater the amplification: more rotational energy is available. This very same reason justifies that $B = 0$ produces no amplification. One also sees that greater amplification occurs for $m = 1$ rather than for $m = 2$. This has to do with the relation between the energy carried by the wave and the potential barrier produced in both cases. A complete explanation can be found in Appendix A of Reference [8]. The results obtained are consistent with previous works, in particular with Figure 2 in Reference [9]. Finally, one observes the reflection factor is never larger than 2. This upper bound is also present in the Reissner–Nordstroem BH and as we will see in the cylindrical setup evaluated later.

### C. Quasinormal modes and stability

If an isolated guitar string vibrates in normal modes, a guitar string coupled to air vibrates in QNMs. In fact, the energy transfer occurring from the string to the surrounding air adds on an imaginary part to the frequency of the (quasi)normal modes. This imaginary part directly accounts for the losses or, in the opposite range of the spectrum, for instabilities associated with the amplification of the wave energy.

Generically, a complex frequency $\omega = \omega_R + i\omega_I$ produces solutions

$$\Psi \sim e^{i\omega_R(r-t)}e^{-\omega_I(r-t)}, \quad (36)$$

where $\omega_R$ influences the phase of the wave and $\omega_I$ modifies its amplitude. Note this is the outgoing part of the wave. Moreover, the sign of $\omega_I$ determines the stability of the solution. A negative $\omega_I$ corresponds to a solution which is damped in time, hence stable. Positive $\omega_I$, on the other hand, is an amplified and thus unstable solution in time.

The QNMs are computed using direct integration a la Chandrasekhar-Detweiler [10]. The results obtained, displayed in Table I, are in accordance with the existing literature.

| $m$ | $\omega_{\rm QNM}$ |
|---|---|
| 1 | $0.4069 - 0.3412i$ |
| 2 | $0.9527 - 0.3507i$ |
| 3 | $1.4685 - 0.3524i$ |
| 4 | $1.9765 - 0.3530i$ |

TABLE I. Fundamental quasinormal frequencies, for $B = 0$.

## IV. DYNAMICS OF ACOUSTIC GEOMETRIES

### A. Wave equation

The new setup consists of fluid surrounding a rotating cylinder. We consider the fluid to be at rest. Taking into account a static fluid configuration, $\mathbf{v_0} = 0$, the wave equation (15) becomes

$$\partial_t^2\psi_1 - \nabla\cdot(c^2\nabla\psi_1) = 0. \quad (37)$$

Using the plane wave equation ansatz given by equation (23), where we identify $R(r) = \frac{\varphi(r)}{\sqrt{r}}$, it reads

$$\partial_r^2\varphi + \left(\frac{\omega^2}{c^2} - \frac{1}{r^2}\left(m^2 - \frac{1}{4}\right)\right)\varphi = 0. \quad (38)$$

### B. Scattering off a rotating cylinder. Superradiance

The cylinder, of radius $R_0$, is characterised by a quantity called acoustic impedance. Its value determines the interaction wall-fluid. The acoustic impedance, $Z$, is a complex variable. The real part is called resistance and the imaginary part is the reactance. The concept of the resistance is similar to that of a regular resistance. Think in terms of Ohm's law. A given material, depending on its resistance, will dissipate more or less energy. The reactance, on the other hand, measures the dephasing during the interaction.

Under the conditions described in Reference [7], $Z_\omega$ can be written as

$$\left(\frac{\partial_r\psi_1}{\psi_1}\right)\Big|_{r=R_0} = -\frac{i\rho_0\omega}{Z_\omega}. \quad (39)$$

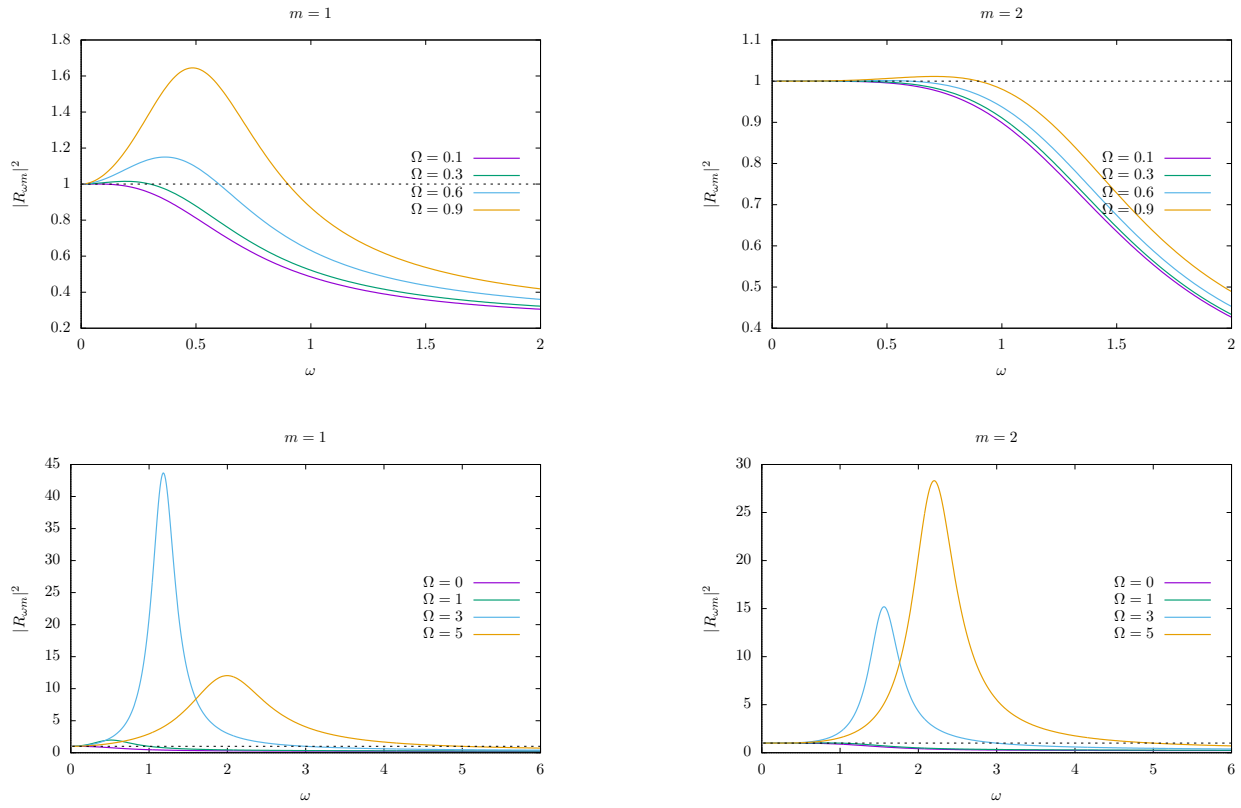


FIG. 3. Reflection coefficient $|R_{\omega m}|^2$ as a function of $\omega$. Several solutions for the differential equation are produced, as one changes the value of parameter $\Omega$, the angular velocity of the rotating cylinder. The left hand panels show the results for $m = 1$ and the right hand ones the results for $m = 2$. $|R_{\omega m}|^2 = 1$ (limit above which superradiance occurs) is plotted as a dashed line. The following parameters were used: $c = \rho_0 = R_0 = 1$ and $Z = 1 - i$. $\Omega$ is presented in units of $c/R_0$.

This equation is the boundary condition one imposes at $r = R_0$. For a cylinder rotating uniformly with angular velocity $\Omega$, the frequency of the incident wave can be modified to include the angular rotation such that

$$\omega \to \tilde{\omega} = \omega - m\Omega. \tag{40}$$

Once again, one faces a Schroedinger-like wave equation and hence one can equate Wronskians at different radial coordinates. Also here the superradiance condition yields the result of equation (34).

Implementing a numerical solution in all similar to the one described in Section III B, one produces the plots of Figure 3. A very obvious distinction between the curves in the two spacetimes has to do with the fact that here the curve never reaches $|R_{\omega m}|^2 = 0$. This is a consequence of the definition of the acoustic impedance, which has been set to $Z = 1 - i$. This value is standard for several known materials [11]. Out of the plots displayed, the maximum amplification for $m = 1$ occurs when $\Omega = 3$ and it corresponds to $|R_{\omega m}|^2 = 43.677$, at $\omega = 1.18$. For $m = 2$, the maximum amplification is at $\Omega = 5$, with $|R_{\omega m}|^2 = 28.314$, at $\omega = 2.20$. The location of the maxima is related to the QNMs – see Figure 5. Note the maximum amplification associated to $m = 1$ is greater than the one to $m = 2$, as usual. Finally, one should mention that when $\Omega = 0$, the curve is always below the dashed $|R_{\omega m}|^2 = 1$ line. In other words, when the cylinder is not rotating, there is no amplification.

The amplification is never larger than $|R_{\omega m}|^2 = 2$ when $\Omega < 1$. Using WKB expansions, one can predict such limit. For a full discussion on the subject cf. Reference [12]. Exiting the realistic range of values for the acoustic impedance, the upper bound of 2 ceases to exist. In fact, there is a tendency that smaller impedances return greater amplifications; and vice-versa. This result makes sense when we think of the nature of impedance, which is that of a resistance. This result is illustrated in Figure 4, where we plot different values of $Z$ for a fixed rotational speed $\Omega = 0.7\ c/R_0$.

### C. Quasinormal modes and stability

In the spirit of studying superradiance-triggered instabilities, one looks at the QNMs of the system. The modes are computed in a slightly different fashion than before. By confining the cylinder, we look at solutions whose frequencies $\omega$ are invariant under changes of such con-

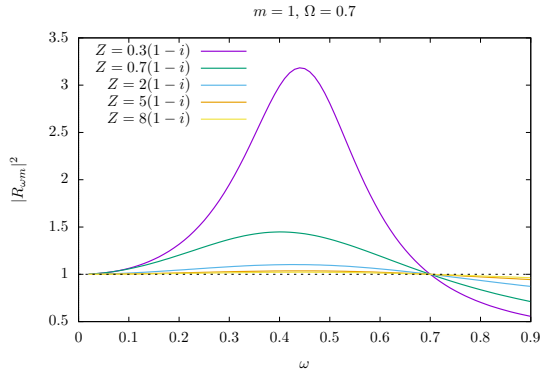


FIG. 4. Reflection coefficient $|R_{\omega m}|^2$ as a function of $\omega$. By keeping the rotation speed of the cylinder constant ($\Omega = 0.7\ c/R_0$), we see how different acoustic impedances influence the reflection coefficient. One can clearly observe that the smaller the impedance, the larger the amplification. Finally, it is interesting to note the superradiant regime ceases to exist as soon as $\omega$ reaches 0.7, as predicted by the superradiance condition ($m\Omega = 0.7$).

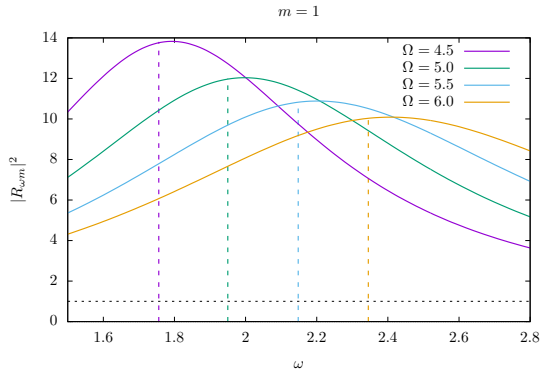


FIG. 5. Reflection coefficient $|R_{\omega m}|^2$ as a function of $\omega$. We focus our analysis in the relation between the maximum amplification factor and $\omega_{\rm QNM}$ by drawing vertical lines that correspond to $\mathrm{Re}(\omega_{\rm QNM})$. The QNMs are drawn in the same colour as the respective reflection curves. $\Omega$ is in units of $c/R_0$.

finement radius. The confinement is achieved by adding a cylinder to our setup. It has radius $R_1 > R_0$ and is concentric with the first one. We impose the outer cylinder to behave as a perfect mirror, reflecting back all incident radiation. The boundary condition in terms of the radial field reads

$$\partial_r \varphi - \frac{\varphi}{2r} = 0. \tag{41}$$

In this configuration, whenever both $\omega_R$ and $\omega_I$ are constant, we have found a QNM. The requirement for constancy of $\omega$ ensures the frequency at infinity to be the same as the one found in the confined setup. Ergo, the frequency found is that characteristic of an open system, a QNM frequency by definition. The results are in Table II. The QNMs are unstable ($\omega_I > 0$), which is not

| $\Omega$ | $\omega_{\rm QNM}$ $(m=1)$ | $\omega_{\rm QNM}$ $(m=2)$ |
|---|---|---|
| 3.0 | $1.1744 + 0.1772i$ | – |
| 3.5 | $1.3669 + 0.2928i$ | – |
| 4.0 | $1.5610 + 0.4050i$ | – |
| 4.5 | $1.7562 + 0.5148i$ | $2.0124 + 0.1912i$ |
| 5.0 | $1.9522 + 0.6228i$ | $2.1845 + 0.3262i$ |
| 5.5 | $2.1487 + 0.7295i$ | $2.3618 + 0.4564i$ |
| 6.0 | $2.3457 + 0.8351i$ | $2.5428 + 0.5825i$ |

TABLE II. Frequencies of QNMs, for $m = 1$ and $m = 2$. The frequencies presented correspond to the fundamental mode. The entries of the table marked with – are those for which we could not find the corresponding $\omega_{\rm QNM}$. We were able to find QNM down to $\Omega = 2.8$ for $m = 1$ and $\Omega = 4.2$ for $m = 2$.

surprising, as the frequencies of Table II correspond to domains where superradiance is present – cf. Figure 3.

Comparing the QNM frequencies displayed in Table II with the plots of Figure 3, one identifies a correspondence between the maximum amplification and the location of the QNMs. See Figure 5, where we have plotted the $|R_{\omega m}|^2$ curves, signalling the QNM frequencies as well.

### D. Confined geometry

Rather than using the confinement as a means of computing QNMs, one examines how it can impact the stability of the solutions. We turn now our attention to the values of $\omega_I$ in subcritical rotational speeds: $\Omega < c/R_0$. As one approaches subsound rotational speeds, $\omega_I$ becomes smaller and smaller. At a certain point, it may even become negative. In fact, for some rotational speeds $\Omega$ and at given ratios $R_1/R_0$, there are stable solutions ($\omega_I < 0$). Working with other values of $\Omega$ and studying where the crossing $\omega_I = 0$ occurs, we obtain the results shown in Figure 6, which fit to $R_1/R_0 = \frac{a}{\Omega}$. $a$ is a free parameter.

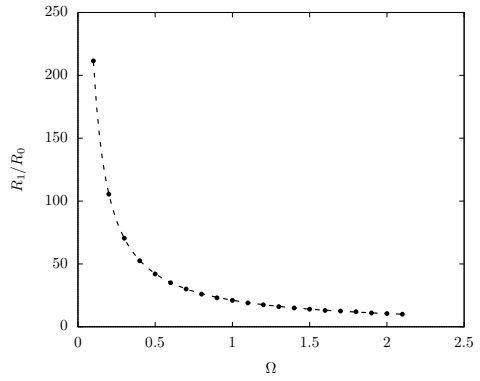


FIG. 6. Coordinates $R_1/R_0$ and $\Omega$ for which $\omega_I = 0$. For increasingly lower rotational speeds, the point where the curve for $\omega_I(R_1/R_0)$ crosses the $\omega = 0$ axis is increasingly higher. The fit equation is $R_1/R_0 = (21.1154 \pm 0.0175)/\Omega$.

To decode the nature of the fit, we can think of the physical consequences of setting $\omega_I = 0$. In the limit of vanishing $\omega_I$, superradiant instabilities are non-existing. More precisely, we are in the regime where $\omega = m\Omega$, $\omega$ being a purely real frequency. Our knowledge of normal

modes allows us to recognise that, given finite boundary conditions, $\omega$ is inversely proportional to the distance between such finite boundaries. In our specific case, we can thus write

$$\frac{1}{R_1/R_0} \sim m\Omega, \tag{42}$$

which is in accordance with the numerical results.

## V. DYNAMICS OF ACOUSTIC GEOMETRIES IN VISCOUS FLOWS

### A. Governing equations and wave equation

Viscosity is a phenomenon of internal friction, which causes an irreversible transfer of momentum from points where the velocity is large to those where it is small. Processes of internal friction occur in a fluid only when different fluid particles move with different velocities, so that there is a relative motion between various parts of the fluid. Including viscosity in the treatment done so far means that a modification of the fluid equations is in order. At this point, we substitute the Euler equation by the Navier-Stokes equation,

$$\rho\, \partial_t \mathbf{v} + \rho\, \mathbf{v}\cdot\nabla\mathbf{v} = -\nabla p + \mu\nabla^2\mathbf{v} + \left(\xi + \frac{\mu}{3}\right)\nabla\left(\nabla\cdot\mathbf{v}\right). \tag{43}$$

This formulation of the Navier-Stokes equation holds for compressible flows, where we require $\mu$ and $\xi$ to be constant throughout the flow. $\mu$ and $\xi$ are, respectively, the dynamic and second (bulk) viscosities of the fluid.

Linearising and following the procedure described in Section II A, we obtain the perturbed version of the Navier-Stokes equation,

$$\partial_t\psi_1 = -\mathbf{v_0}\cdot\nabla\psi_1 - \frac{p_1}{\rho_0} + \frac{\alpha}{\rho_0}\left(\nabla^2\psi_1 - \frac{\rho_1}{\rho_0}\nabla\mathbf{v_0}\right), \tag{44}$$

where $\alpha$, the viscosity parameter, is defined as $\alpha = \xi + \frac{4}{3}\mu$. The corresponding wave equation reads

$$\partial_t\left\{\partial_t\psi_1 + \mathbf{v_0}\cdot\nabla\psi_1 - \frac{\alpha}{\rho_0}\nabla^2\psi_1\right\} + \nabla\cdot\left\{-c^2\nabla\psi_1 + \mathbf{v_0}\left(\partial_t\psi_1 + \mathbf{v_0}\cdot\nabla\psi_1 - \frac{\alpha}{\rho_0}\nabla^2\psi_1\right)\right\} = 0. \tag{45}$$

In this equation we have used the fact that the background flow is irrotational, $\nabla\times\mathbf{v} = 0$, and incompressible, $\nabla\cdot\mathbf{v_0} = 0$.

Making use of the plane wave ansatz (23) and working once more in a static fluid configuration, one obtains the wave equation in terms of the radial field,

$$\partial_r^2\varphi + \left(\frac{\omega^2}{c^2 - i\omega\alpha/\rho_0} - \frac{1}{r^2}\left(m^2 - \frac{1}{4}\right)\right)\varphi = 0. \tag{46}$$

It can be noticed viscosity is only relevant when dealing with high frequencies $\omega$. The viscous term can be thought of as a correction to the local speed of sound. We define an effective local speed of sound, as

$$c_{\text{eff}}^2 = c^2 - i\frac{\omega\alpha}{\rho_0}. \tag{47}$$

In view of analysing the role of viscosity in the analogue treatment, we first derive its units. Secondly, we define the range of realistic values in such units. Numerically, we work with $c = \rho = 1$. This choice is equivalent to rescaling the quantities

$$\hat{\omega} = \frac{\omega}{c}, \qquad \hat{\alpha} = \frac{\alpha}{c\rho_0}. \tag{48}$$

Dimensional analysis yields

$$[\alpha] = \frac{\text{M}}{\text{LT}} \tag{49}$$

$$[\hat{\alpha}] = \text{L}, \tag{50}$$

where M is a mass unit, L stands for length and T for time. In the new units, viscosities of realistic fluids are in the range

$$\hat{\alpha} \in [10^{-10}, 10^{-5}]\ \text{cm}. \tag{51}$$

The choice of cm as length unit has to do with the experimental realisation of the setup; in particular with $R_0 = 1$ cm. For the remainder of the article, all hats are dropped and we work with the rescaled quantities.

### B. Scattering in the presence of viscosity

Working with the viscous wave equation (45), one starts by realising that the effective potential in the wave equation is complex. Consequently, the Wronskian is not constant in the radial coordinate [13]. Instead, it obeys

$$\frac{dW}{dr} = 2i\frac{\alpha\omega^3}{\rho c^4 + \frac{\omega^2\alpha^2}{\rho}}|\varphi(r)|^2. \tag{52}$$

This leads to a modified condition for the reflection coefficient $|R_{\omega m}|^2$ in viscous superradiant systems:

$$\omega < m\Omega \implies |R_{\omega m}|^2 > 1 - \alpha\omega^2. \tag{53}$$

Identically to the previous sections, we plot the reflection coefficient $|R_{\omega m}|^2$ as a function of the frequency $\omega$ – Figure 7. We work with $\Omega = 0.9$ and $\Omega = 3$ for both $m = 1$ and $m = 2$, while varying the values of $\alpha$ in

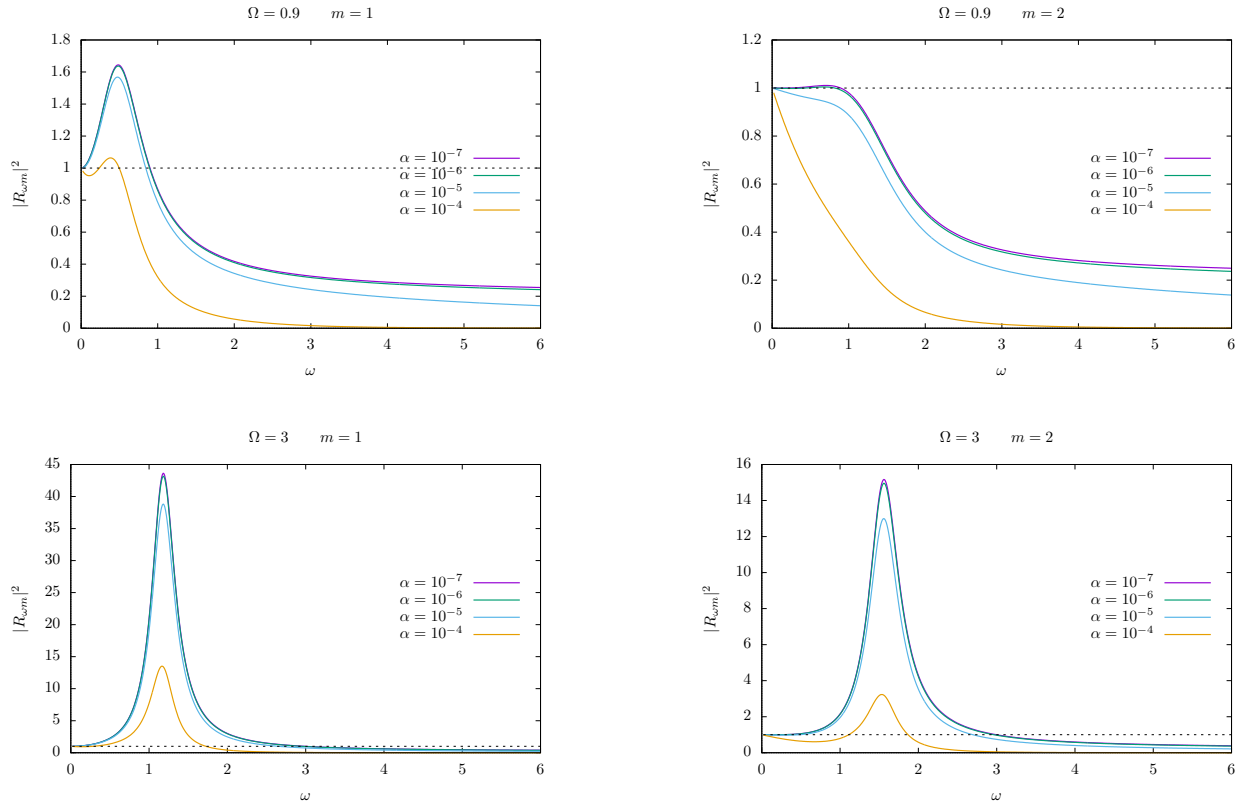


FIG. 7. Reflection coefficient $|R_{\omega m}|^2$ as a function of $\omega$. The plots presented here provide the modified solutions to Figure 3. For each pair of parameters $(\Omega, m)$, several orders of magnitude of $\hat{\alpha}$ are studied. We observe increasing viscosity yields less amplification. In the range of viscosities of real fluids and the frequencies $\omega$ considered, the superradiant limit is, in good approximation, $|R_{\omega m}| = 1$. As usual, we plot the limit above which superradiance occurs as a dashed line.

accordance with the real fluids range presented in equation (51). One observes greater viscosity returns less amplification. This was to be expected, as a viscous fluid behaves as a dissipative means for energy. In order to quantitatively assess how viscosity impacts the reflection coefficient, one can compute the areas associated with the various curves of Figure 7. Posterior normalisation with respect to the non-viscous case produces the results displayed in Figure 8.

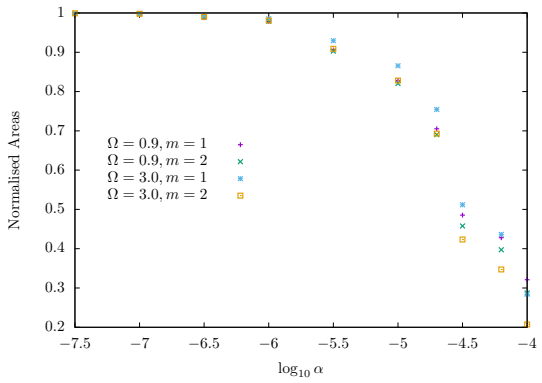


FIG. 8. Area normalisation. For the same $\Omega$, viscosity's impact is higher for $m = 2$. One should pay special attention to the case where $\alpha = 10^{-7}$, as the ratio area with viscosity to area with no viscosity is virtually 1. This validates our previous approach of assuming water to have null viscosity. Note water has a viscosity of order of magnitude $10^{-8}$.

### C. Quasinormal modes. Superradiant instabilities in the presence of viscosity

Starting with the already known results for the non-viscous case, displayed in Table II, and increasing $\alpha$ up to several orders of magnitude, one observes $\omega_I$ decreases as viscosity increases. This behaviour is in agreement with the results of Figure 7, as smaller values of $\omega_I$ mean less amplification. However, these modifications to the QNMs frequencies due to viscosity occur only for orders of magnitude greater than $\alpha \sim 10^{-3}$. Hence, the QNMs frequencies of real fluids suffer no relevant changes due to viscosity.

### D. Confined geometry in the presence of viscosity

Running the same parameters as in Section IV D, with $\alpha \neq 0$, one observes that, in the range of realistic viscosities, no modifications arise. Due to the constancy of the plots, we assume the fit of Figure 6 for the case of no viscosity to hold here as well. One concludes the behaviour of the frequencies for subcritical velocities is independent of viscosity, in the domain of real fluids.

## VI. FINAL REMARKS

Albert Einstein's GR is a colossal achievement of 20th-century physics. The claim that what we perceive as the force of gravity actually arises from the curvature of spacetime is not a straightforward one. The scientific paradigm Einstein introduced is still present nowadays, with GR being our best candidate for a theory of gravity. Since its initial publishing, GR has been subjected to many experimental tests. The most recent triumph was in 2015 with the detection of gravitational waves, a century after their initial prediction. GR is a very hard theory to test at will. Besides its mathematically challenging predictions, the experimental tests must be done under very specific conditions. Tests of strong-field gravity, for instance, can only be performed near astrophysical bodies such as BHs and neutron stars. Probing this type of results is not an easy task and it often deems itself impossible due to technological lags.

Acoustic analogues bridge the gap between theory and experiment, as they allow for the testing of phenomena – as Hawking radiation and superradiance, to name but a few – one would not be able to otherwise. Such effects are virtually impossible to study in astrophysical BHs with the existing technology.

Studying two distinct setups, we introduced the reader to the analogue framework whilst producing new results on the topic. In particular, we saw horizons are not a necessary condition for superradiance. On top of that, we successfully concluded on how viscosity affects the superradiance results in the cylinder geometry.

## ACKNOWLEDGMENTS

S. Freitas would like to thank Professor Dr. Vítor Cardoso for all the good advice, geniality, perfectionism and knowledge. The completion of this work would have not been possible without his guidance.

[1] F. W. Dyson, A. S. Eddington, and C. Davidson. A determination of the deflection of light by the sun's gravitational field, from observations made at the total eclipse of may 29, 1919. *Philosophical Transactions of the Royal Society of London A: Mathematical, Physical and Engineering Sciences*, 220(571-581):291–333, 1920. ISSN 0264-3952. doi:10.1098/rsta.1920.0009.

[2] B. P. Abbott et al. Observation of Gravitational Waves from a Binary Black Hole Merger. *Phys. Rev. Lett.*, 116 (6):061102, 2016. doi:10.1103/PhysRevLett.116.061102.

[3] K. Schwarzschild. On the gravitational field of a mass point according to Einstein's theory. *Sitzungsber. Preuss. Akad. Wiss. Berlin (Math. Phys.)*, 1916:189–196, 1916.

[4] W. G. Unruh. Experimental black hole evaporation. *Phys. Rev. Lett.*, 46:1351–1353, 1981. doi: 10.1103/PhysRevLett.46.1351.

[5] T. Torres, S. Patrick, A. Coutant, M. Richartz, E. W. Tedford, and S. Weinfurtner. Observation of superradiance in a vortex flow. 2016.

[6] R. Schutzhold and W. G. Unruh. Gravity wave analogs of black holes. *Phys. Rev.*, D66:044019, 2002. doi: 10.1103/PhysRevD.66.044019.

[7] V. Cardoso, A. Coutant, M. Richartz, and S. Weinfurtner. Detecting Rotational Superradiance in Fluid Laboratories. *Phys. Rev. Lett.*, 117(27):271101, 2016. doi: 10.1103/PhysRevLett.117.271101.

[8] S. Freitas. Acoustic black holes and superressonance mechanisms. Master's thesis, Técnico Lisboa, 10 2017.

[9] E. Berti, V. Cardoso, and J. P. S. Lemos. Quasinormal modes and classical wave propagation in analogue black holes. *Phys. Rev.*, D70:124006, 2004. doi: 10.1103/PhysRevD.70.124006.

[10] S. Chandrasekhar and S. Detweiler. The quasi-normal modes of the Schwarzschild black hole. *Proc.Roy.Soc.Lond.A344*, pages 441–452, 1975.

[11] M. Delany and E. Bazley. Acoustical properties of fibrous absorbent materials. *Applied Acoustics*, 3(2):105 – 116, 1970. ISSN 0003-682X. doi: http://dx.doi.org/10.1016/0003-682X(70)90031-9.

[12] V. Baibhav, V. Cardoso, and R. Emparan. Universal bounds on superradiance (unpublished).

[13] M. Richartz, S. Weinfurtner, A. J. Penner, and W. G. Unruh. General universal superradiant scattering. *Phys. Rev.*, D80:124016, 2009. doi: 10.1103/PhysRevD.80.124016.